CrossMark

High Power Laser Science and Engineering, (2023), Vol. 11, e41, 10 pages.
doi:10.1017/hpl.2023.35

HIGH POWER LASER SCIENCE AND ENGINEERING

RESEARCH ARTICLE

Laser pulse shape designer for direct-drive inertial confinement fusion implosions

Tao Tao[1], Guannan Zheng[1], Qing Jia[1], Rui Yan[2,3], and Jian Zheng[1,3]

[1] *Department of Plasma Physics and Fusion Engineering and CAS Key Laboratory of Geospace Environment, University of Science and Technology of China, Hefei, China*

[2] *Department of Modern Mechanics, University of Science and Technology of China, Hefei, China*

[3] *Collaborative Innovation Center of IFSA, Shanghai Jiao Tong University, Shanghai, China*

(Received 10 February 2023; revised 22 March 2023; accepted 17 April 2023)

Abstract

Pulse shaping is a powerful tool for mitigating implosion instabilities in direct-drive inertial confinement fusion (ICF). However, the high-dimensional and nonlinear nature of implosions makes the pulse optimization quite challenging. In this research, we develop a machine-learning pulse shape designer to achieve high compression density and stable implosion. The facility-specific laser imprint pattern is considered in the optimization, which makes the pulse design more relevant. The designer is applied to the novel double-cone ignition scheme, and simulation shows that the optimized pulse increases the areal density expectation by 16% in one dimension, and the clean-fuel thickness by a factor of four in two dimensions. This pulse shape designer could be a useful tool for direct-drive ICF instability control.

Keywords: double-cone ignition; hydrodynamics instability; machine-learning optimization; pulse shape optimization

1. Introduction

Inertial confinement fusion (ICF)[1–3] uses drivers such as lasers to implode a fuel-containing shell, compress it to extreme conditions[3] and trigger a sustained thermonuclear reaction. However, the acceleration of the shell creates favorable conditions for the development of Rayleigh–Taylor instability (RTI)[4,5], which can lead to severe ablator–fuel mixing and even shell breakup[6,7]. Direct-drive ICF[2] is particularly susceptible to RTI, because the laser imprint[8] can couple illumination non-uniformities directly to the shell, providing a large number of seeds for RTI. Measures to suppress the imprint include target roughness reduction[9], beam overlap optimization[10,11], beam smoothing[12] and pulse shaping[13,14].

Pulse shaping is a powerful tool for mitigating instabilities. For example, isentropic pulses[15] can achieve the maximum density compression in an idealized 1D implosion, but the risk of instability is high. Components such as intense 'pickets'[13] (power spikes) are added to the main pulse to help adjust the plasma density profile and reduce the instability seed due to the laser imprint. Well-shaped pulses can achieve the effect of 'adiabat shaping'[16]: a picket-driven decaying shock[17] heats only the outer layer of the shell (high adiabat) to effectively smooth the imprint, while the inner layer of the shell remains relatively cold (low adiabat) to preserve the density compressibility.

However, pulse design is not straightforward. The relationship between pulse shapes and implosion performance is nonlinear and depends on the imprint details, which is facility-specific. Algebraic metrics such as the ignition threshold factor (ITF)[18,19] lack the modeling of the imprint details, while experiments reflect all the instabilities but are very expensive. For these reasons, effective pulse design relies heavily on numerical and statistical models.

Recently, data-driven methods[20–27] have shown great potential in ICF research. For example, evolutionary algorithms can automate the exploration of pulse shapes and target geometries, and generate new classes of implosion designs[21–23]. Regression and classification algorithms can identify the complex correlations between the experimental inputs and outputs[21,24,25], and help increase the experimental neutron yield[26]. Transfer learning uses a

Correspondence to: Jian Zheng, Department of Plasma Physics and Fusion Engineering and CAS Key Laboratory of Geospace Environment, University of Science and Technology of China, Hefei 230026, China. Email: jzheng@ustc.edu.cn

© The Author(s), 2023. Published by Cambridge University Press in association with Chinese Laser Press. This is an Open Access article, distributed under the terms of the Creative Commons Attribution licence (https://creativecommons.org/licenses/by/4.0), which permits unrestricted re-use, distribution and reproduction, provided the original article is properly cited.

https://doi.org/10.1017/hpl.2023.35 Published online by Cambridge University Press

small high-fidelity dataset to calibrate the naive prediction trained on a much larger low-fidelity dataset, which is ideal for merging simulation and experimental observations[27,28].

In this research, we develop an automated pulse shape designer for direct-drive schemes. The pulse designer uses machine-learning algorithms to evolve the pulse shapes for higher compression density and better implosion stability. The facility-specific imprint characteristics are considered in the optimization, making the pulse shaping more relevant. This designer is tested on the novel double-cone ignition (DCI) scheme[29]. Simulation shows that the optimized pulse increases the baseline areal density by 16% and increases the clean-fuel thickness by a factor of four. At the same time, the robustness of the pulse against shaping errors is also evaluated.

The paper is organized as follows. Section 2 introduces the simulation setup and optimization workflow. Section 3 introduces the RTI linear growth prediction. Section 4 introduces the implosion performance surrogate (IPS) model. Section 5 introduces the model correction by imprint seeds. Section 6 introduces the pulse quality check. Section 7 is a summary.

2. Simulation setup and optimization workflow

The DCI target is a shell-in-cone design, as shown in Figure 1(a). The cone half-angle is 50° (polar angle), the small hole radius is 50 μm and the double-cone separation is 100 μm. The shell composition is high-density plastic (1.27 g/cm^3, C:H=1:1). The shell inner radius $r_i = 450$ μm and the outer radius $r_o = 495$ μm. Each cone is illuminated by four laser beams, the beam incident angle is 50°, each beam delivers 1.5 kJ of energy (12 kJ in all beams) and the laser wavelength is $\lambda_L = 351$ nm. Figure 1(c) shows the power intensity of the laser spot; the inhomogeneous speckle feature is modeled and the speckle power root-mean-square value is $\sigma_{rms} \sim 15\%$.

We use two radiation hydrodynamics codes in our work. The first one is the Lagrangian code MULTI-1D[30], which models the DCI target in spherical geometry and resolves the implosion on the radial dimension only. The second is the Eulerian code FLASH[31], which models the DCI target in 2D cylindrical geometry and resolves the instability evolution. The laser speckle is modeled only by the FLASH code.

In an ideal DCI implosion, the shells experience compression, acceleration and extrusion (from the cone hole). After that, the head-on flying shells collide and stagnate, forming a high-density fuel package ready to be ignited by relativistic electron beams[29]. However, hydrodynamic instability poses a serious threat, as demonstrated by the FLASH example in Figure 1(e). An isentropic pulse[15] is used to drive the implosion, and such a pulse can achieve the maximum density compression in one dimension for a given laser energy. However, without any pulse shaping, the shell is easily imprinted by the speckle, generating short-wavelength perturbations. These perturbations seed the rapid development of acceleration RTI, and almost break the shell before extrusion.

We design a pulse optimization workflow to tune the pulse shape, as shown in Figure 2. The workflow consists of four main components: the IPS, 1D simulations, 2D simulations and a pulse production and quality check. The pulse shape is optimized by iterating this workflow.

The meaning of the IPS should be clarified first. A surrogate is a data-driven model used to represent the complex input and output relationships of a system when a simple algebraic representation is not available. In our case, due to the complexity of implosions, the relation IPS(P) is not known. Here, P represents the pulse parameters. However, we can write IPS = IPS(ρ_a, A) in a heuristic form (see

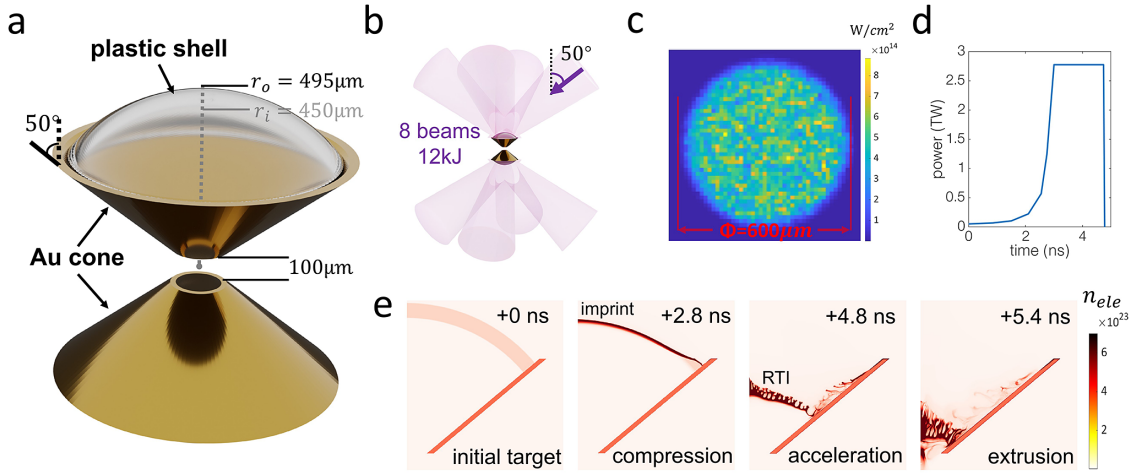

Figure 1. (a) Schematic of the DCI target. (b) Schematic of the incident laser beams. (c) Power intensity of a single laser spot with inhomogeneous 'speckle' feature. (d) An isentropic pulse shape used in the example simulation to show (e) the density distribution at four DCI implosion stages: initial target, compression, acceleration and extrusion. This simulation is conducted in cylindrical geometry and only resolves half of the upper-cone.

https://doi.org/10.1017/hpl.2023.35 Published online by Cambridge University Press

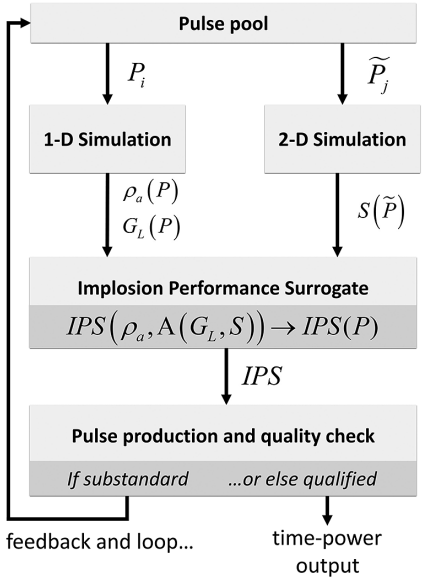

Figure 2. Pulse shape designer workflow, where the primary goal is to maximize the implosion performance surrogate.

Section 4), where ρ_a is the areal density and A is the maximum perturbation amplitude. The goal of the optimization is to adjust P so that the IPS is maximized.

After defining the IPS, simulations are performed to obtain ρ_a and A. The fluid variables can be obtained by 1D simulations, from which we can calculate the stagnation areal density ρ_a and the RTI growth multiplier G_L(see Section 3). The imprint seed S can be obtained by 2D simulations, and the instability amplitude can be inferred as $A = SG_L$.

Machine-learning algorithms are used to build the IPS. Specifically, classification and clustering algorithms are used in the 'prediction–correction' steps. In the prediction step, a machine-learning classifier is trained on the $P-$IPS data sampled in one dimension, and the classification helps to improve the prediction on G_L. In the correction step, a machine-learning cluster is used to identify good pulse commonalities and sample their imprint patterns, and clustering helps update the seed S (see Section 5). The optimization algorithm is implemented using the MATLAB language and its machine-learning toolkit.

Pulse production determines the best pulse shape from the IPS. The pulse quality check tests the pulse's compression, implosion stability and robustness (see Section 6). If the pulse meets the engineering requirements, its time-power data is output. Otherwise, one loops and continues sampling the pulse space.

3. Rayleigh–Taylor instability linear growth prediction

The continuous pulse is decomposed into finite nodes, node power pw and node timing dt can change freely and a pulse space is constructed based on these finite

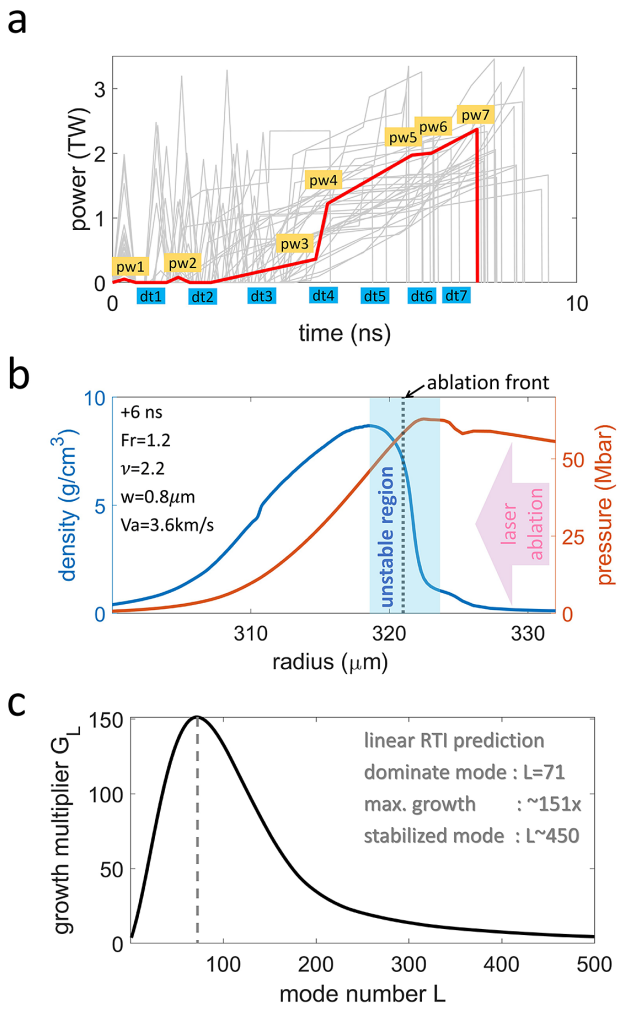

Figure 3. (a) The pulse shape is decomposed into a finite number of nodes. The example pulse is marked with node power pw and node timing dt. Changing the node values generates many other pulse shapes in the same pulse space, as shown by the grey lines. (b) Implosion density and pressure profile of the example pulse at +6 ns. Fitting these profiles to obtain the RTI growth parameters. (c) Calculated RTI growth multiplier of the example pulse.

degrees of freedom (DoFs). Each shape is a unique point with coordinates $[\mathrm{pw1}, \mathrm{dt1}, \mathrm{pw2}, \mathrm{dt2}\ldots]$ in the pulse space. Figure 3(a) shows a pulse series with two pickets preceding the main acceleration (the picket width is 500 ps, the pulse length limit is 10 ns and the power ceiling is 6 TW). The pickets are forced by limiting the power of several nodes to 0. The purpose of the first picket is to resist the imprint, and the purpose of the second picket is to work with the acceleration pulse (main pulse) to reach higher compression. A 14D pulse space is needed to describe such a pulse shape. We randomly select an example pulse shape in Figure 3(a) and estimate its corresponding RTI linear growth.

The ablation front is detected at each evolution step in the 1D implosion, and the region with opposite density and pressure gradient is delineated as RTI unstable. Figure 3(b) shows the unstable region at +6 ns. The instantaneous

https://doi.org/10.1017/hpl.2023.35 Published online by Cambridge University Press

growth rate γ is calculated using the steady-state equation of Betti *et al.*[32]:

$$\gamma = \sqrt{\alpha_1(\nu,\epsilon)\,kg + \alpha_2(\nu,\epsilon,F_r)\,k^2V_a^2} - \beta_1(\nu,\epsilon)\,kV_a, \quad (1)$$

where k is the wave vector, g is the effective acceleration, V_a is the ablation velocity, ν is the power index of heat conduction ($\nu = 2.5$ for electron conduction), w is the characteristic width of the ablation front, $F_r = V_a^2/(gw)$ is the Froude number and α_1, α_2 and β_1 are complex functions that can be found in Betti *et al.*'s work. The values of ν, w, F_r and V_a can be determined by fitting density and pressure profiles in the unstable region. The annotation in Figure 3(b) shows the fitted values at the instant moment +6 ns. Acceleration g is calculated by tracking the center of the mass trajectory of the shell. Integrate instant γ over time slices Δt to obtain the growth multiplier $G_L = \exp(\gamma_{1L}\,\Delta t_1 + \gamma_{2L}\,\Delta t_2 + \cdots + \gamma_{nL}\Delta t_n)$. Subscript L represents a single circular mode $L = kr$, where r is the radius of the shell. The peak RTI mode and the stabilization mode corresponding to the example pulse are shown in Figure 3(c).

A prerequisite for using the RTI scaling law is that the ablation has already reached a steady-state, that is, the density and pressure profile are quasi-stable. Most of the RTI growth occurs during the acceleration, when the plasma corona is largely established, and the fluid field can quickly adapt to the pulse power change. Although the steady-state ablation assumption does not hold for pickets, the shell acceleration is small, so the picket's contribution to RTI is also small according to Equation (1), resulting in a negligible error. Overall, this time-integrated RTI estimation is generally acceptable.

4. Implosion performance surrogate model

To evaluate the quality of the implosion, a heuristic IPS expression based on DCI physics is given:

$$\mathrm{IPS}(\rho_a, A) = \left\{1 - 2/\left[1 + \exp\left(\rho_a/0.7\ \mathrm{g\cdot cm^{-2}}\right)\right]^2\right\} \cdot \exp\left[-(A/3\ \mu\mathrm{m})^2\right]. \quad (2)$$

The first line on the equation right-hand side is related to density compression. The basic requirement for compression is $\rho_a > 0.3$ g/cm^2 to support alpha self-heating, and the advanced requirement for compression is $\rho_a > 0.8$ g/cm^2 to stop the fast ignition electrons[29]. The second line on the equation right-hand side is related to instability. The basic requirement for instability is $A \sim 3$ μm which is the typical amplitude of the imprint pattern, and the advanced requirement for instability is $A \sim 1.5$ μm such that the perturbation is reduced by half. Based on the DCI physics, we choose 0.7 g/cm^2 and 3 μm in the IPS expression to reflect the trade-off between compression and stability; both factors are associated with term values in the range of 0−1. The IPS mesh is shown intuitively in Figure 4(a). Satisfying the basic requirements results in an IPS ~ 0.25, while satisfying the advanced requirements results in an IPS ~ 0.7.

A classification algorithm is used to build the surrogate. First, we randomly sample the pulse space; we use the word 'batch' to refer to all the pulses in the same optimization loop. Second, we perform 1D simulations on the batch to obtain the IPS scores. In our practice, each batch contains 2000 $P-$IPS relations. We specify a 'filter' threshold for each batch, the scores above/below the threshold are assigned labels T (true)/F (false), thus forming a labeled training set. Then we train a Gaussian kernel support vector machine (SVM)[33] on this training set; after training, the surrogate can predict the pulse performance based on the input P. Note that we use classification rather than regression to build the surrogate, because our tests show that the regression variance is too large in sparsely sampled pulse spaces, and therefore the $P-$IPS is easily overfitted and the prediction by regression is poor.

The filter threshold is slightly elevated between optimization batches for the purpose of pulse evolution. For a new batch, its pulse candidates are first filtered by the

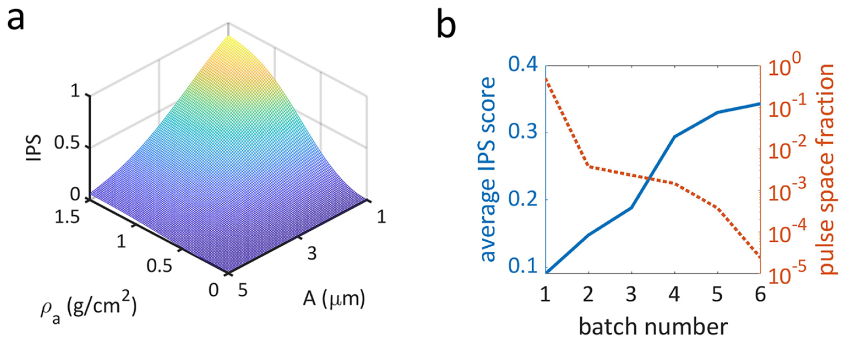

Figure 4. (a) The IPS mesh shape, plotted against areal density ρ_a and perturbation amplitude A. (b) Six consecutive optimization batches, each batch containing 2000 pulse samples; complete optimization uses six batches. The left-hand axis shows the batch-averaged IPS score and the right-hand axis shows the pulse space fraction occupied by each batch.

https://doi.org/10.1017/hpl.2023.35 Published online by Cambridge University Press

classifier from the previous batch, and those pulse candidates predicted true are kept in the simulation pool, while those predicted false are discarded. As the boundary of high-performance pulses slowly becomes clear, we operate the surrogate to produce the best pulse shape. The best pulse can be determined by simply taking the batch high-score or by searching the surrogate. Note that the pulse evolution does not use a common evolutionary algorithm, mainly because the IPS score depends on the imprint seed S, and S is recalibrated before each batch run (detailed in the next section); as a result the extremes of the optimization problem are constantly changing. Therefore, we do not use an evolutionary algorithm, but instead focus on sampling the pulse space more evenly.

Figure 4(b) shows six consecutive batches; their filter thresholds are 0.1, 0.15, 0.2, 0.25, 0.275 and 0.3. The last batch occupies 2×10^{-5} of the whole pulse space; the top 10% pulses achieve compression $\rho_a > 0.5$ g/cm^2 and instability amplitude $A < 2$ μm, demonstrating the effectiveness of the algorithm.

5. Model correction by imprint seeds

The surrogate is corrected by updating the imprint seed S. The imprint is simulated by 2D FLASH code. We modify the FLASH laser module to reflect the real DCI target and laser signatures: the target surface roughness is $\Delta_{\text{std}} = 45$ nm, the laser speckle power non-uniformity is $\sigma_{\text{rms}} \sim 15\%$ and the speckle spectrum peaks at $L \sim 150$ ($\lambda \sim 20$ μm). The FLASH simulations are performed in 2D cylindrical geometry. Examining the imprint for every pulse in the batch is not easy due to the 2D computational load, so we use a clustering method to determine several key pulses and extract their seed features, and we use an interpolation method to synthesize the seeds for other pulse samples.

As explained earlier, each pulse shape is a unique point in the pulse space, the classification algorithm divides points with high IPS scores into discriminative groups and the division minimizes the sum of distances between points and their group centers. Here we use the K-means clustering algorithm[34] and the number of groups K is a free parameter, in our case $K = 9$. Figure 5(a) provides an illustration of the clustered centers c1–c9, while Figure 5(b) shows the imprint simulation of the c9 pulse. Six batches require five rounds of correction and 45 center pulses in total, and their imprint spectrum is obtained by using wavelet analysis on the center-of-mass perturbation of the flying shell when the shell reaches two-thirds of its initial radius.

For a newly sampled pulse, its seed $S(\tilde{P})$ can be interpolated as follows:

$$S\left(\tilde{P}\right) = \sum_k S_k \frac{||\tilde{P} - c_k||^{-2}}{\sum_j ||\tilde{P} - c_j||^{-2}}, \tag{3}$$

where S_k is the spectrum of the centers, c is the coordinates of the centers ($\tilde{P}$ and c are in the same pulse space) and the fractional term is the summation weight. Figure 5(c) shows the interpolated seed for the example pulse in Figure 3(a); the prediction of the instability changes significantly after correction. Figure 5(d) shows the prediction of the dominant mode shifted from $L = 71$ without correction to $L = 37$ with correction, which is much closer to the 2D simulation facts.

We use a validation set consisting of nine newly generated pulses, and compare the interpolation method with the 2D simulation results. Figures 5(e) and 5(f) show that the corrected surrogate has a high correlation with the 2D simulation in both the imprint seed spectrum and the dominant growth mode, confirming the effectiveness of the correction.

6. Pulse quality check

This section describes the pulse quality check. The optimized pulses are evaluated in three aspects: first, the implosion performance improvement over the baseline; second, robustness to shaping errors; and third, optimization results with and without imprint correction.

6.1. Improvement over the baseline pulse

The pulse shape used in the DCI experiment (round 6, starts from winter of 2021) is shown in Figure 6(a). The pulse is a near-isentropic design with a 1D areal density expectation of $\rho_a = 0.95$ g/cm^2. This pulse is used as a baseline for reference. At 2–3.5 ns, the pulse drives a strong shock into the shell and achieves a relatively high in-flight aspect ratio (IFAR, defined as the compressed fuel thickness divided by the initial radius) of approximately 20. The perturbation pattern on the outer surface can be seen in Figure 6(b), where the plasma corona scale length is too short to smooth the speckle at $L \sim 150$ ($\lambda \sim 20$ μm). The seeds are amplified and evolve into the nonlinear phase at the end of the acceleration. The bubbles (low-density region in the instability structure) reach the inner surface of the fuel, with $L \sim 45$ being the dominant mode. The average adiabat of the cold fuel (sampling point along the shell mass center) is kept low at $\alpha = 2.3$, but the fingers with the high adiabat $\alpha = 13.1$ penetrate deeply and contaminate the inner fuel. The unmixed-fuel width is less than 5 μm. The hydrodynamic efficiency (the fraction of laser energy converted to shell energy) of this pulse is 9.2%.

The designer optimizes the acceleration pulse after 12,000 samples. The pulse shape is shown in Figure 6(d). The laser power rises rapidly to 1.8 TW before the first shock reaches the inner surface and then remains steady for 2.2 ns, during which the shell is not further compressed. The pulse power rises to 5 TW at the very end, producing a final boost. The imprinted seeds are neutralized by strong mass ablation,

https://doi.org/10.1017/hpl.2023.35 Published online by Cambridge University Press

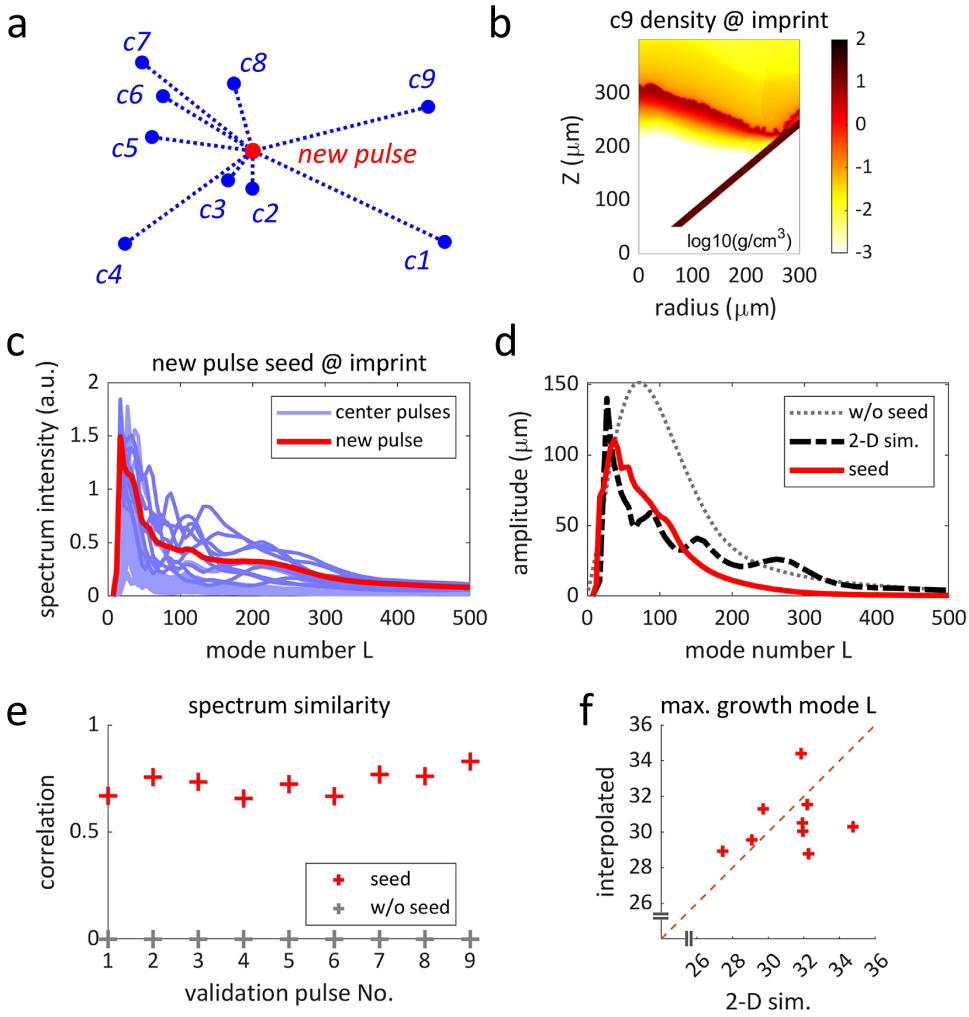

Figure 5. (a) Illustration of a new pulse point and its distance to the center pulse points. (b) Imprint density of the c9 center pulse. (c) Seed spectrum interpolation for the new pulse. (d) Instability amplitude of the new pulse, with seed correction, without seed correction and the 2D simulation amplitude. (e) Correlation between the interpolated seed spectrum and the 2D simulated spectrum. (f) Dominant mode in the interpolated spectrum and the 2D simulated spectrum.

and the accelerated RTI is mitigated by a prolonged hot corona. The shell remains intact, and there are no significant short-wavelength or medium-wavelength perturbations in the density or adiabat. This pulse reaches an areal density $\rho_a = 0.83$ g/cm^2, IFAR $\sim$ 10 and a slightly high adiabat $\alpha = 3.9$. This pulse sacrifices compression for stability. The hydrodynamic efficiency of this pulse is 8.4%.

The designer performs best when pickets are allowed, as shown in Figure 6(g). A low-intensity picket produces thin plasma at the fuel surface. A second higher picket sends a stronger shock into the fuel. The acceleration pulse switched on immediately after the pickets. These three shocks reach the inner layer synchronously; IFAR $\sim$ 15. One dimension predicts $\rho_a = 1.1$ g/cm^2; this is the best value among all the three pulses. More importantly, the outer layer perturbation is much less developed due to a well-established plasma corona before 3.5 ns. The bubbles develop at the final acceleration but do not penetrate the inner fuel. In Figure 6(i), the unmixed fuel remains cold ($\alpha = 3.2$) and sufficiently thick (> 20 μm). The velocity of the shell before exiting the cone is $V \sim 190$ km/s. The hydrodynamic efficiency of the picket pulse is 10.8%.

The areal density is overestimated in one dimension. Taking the acceleration pulse as an example, the FLASH 2D areal density at stagnation is $\rho_a = 0.27$ g/cm^2, which is only 33% of the 1D value. However, this does not affect the surrogate, since the implosion degradation due to instability is reflected individually (as a correction to the 1D prediction).

The advantageous shaping strategy of the two-picket pulse is reflected in Figure 7(a). The first picket delivers less than 1% of the total energy, allowing the shell outer surface to expand for approximately 2 ns, forming a corona with $D_{ac} >$ 20 μm; this length is comparable to a typical laser speckle. The illumination non-uniformity decays exponentially over the long distance from the critical surface to the ablation front. The second picket starts the compression in an imprint-

https://doi.org/10.1017/hpl.2023.35 Published online by Cambridge University Press

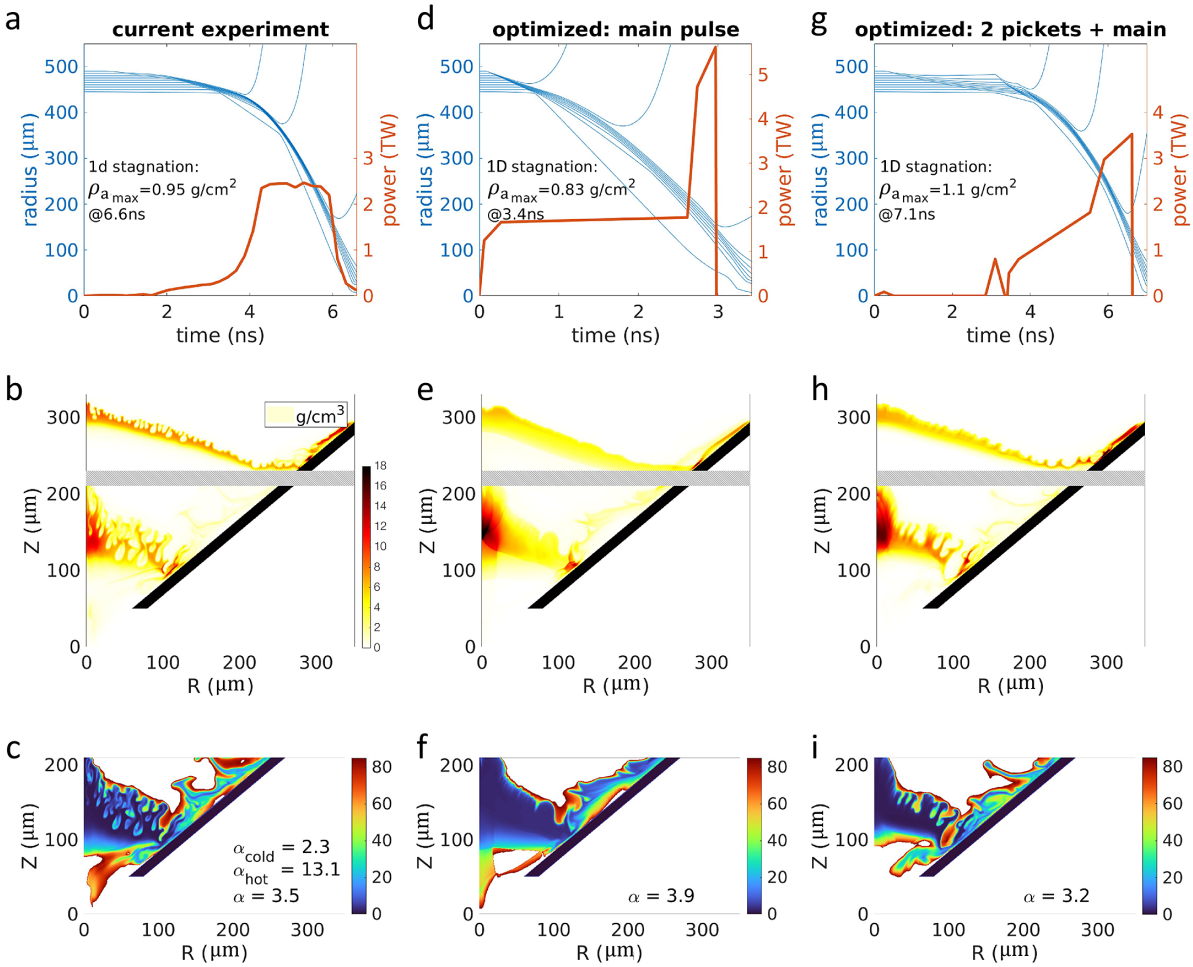

Figure 6. Implosion simulation of (a)–(c) the baseline pulse, (d)–(f) the designer-optimized acceleration pulse and (g)–(i) the designer-optimized two-picket pulse. The first row of the figure shows the respective pulse shapes and 1D implosion streamlines. The second row shows the shell's density at two-thirds and one-third of its initial radius. The third row is the adiabat of the shell at one-third of its initial radius.

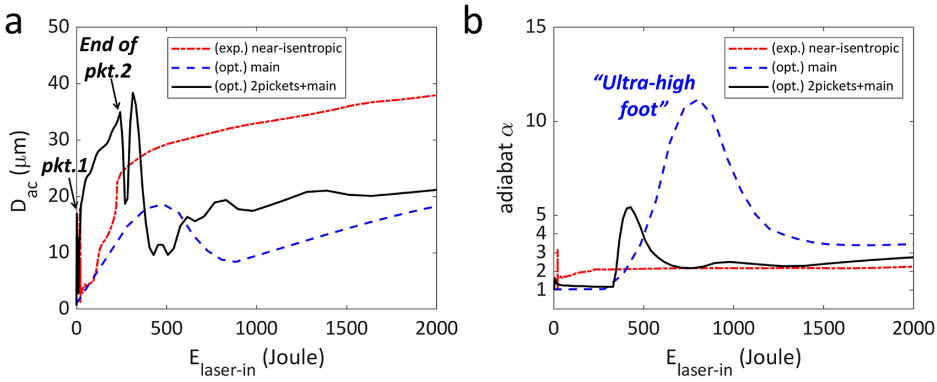

Figure 7. (a) Time evolution of D_{ac}, the distance between the ablation front and the critical surface. (b) Time evolution of the fuel adiabat α. The horizontal axis is the laser energy delivered; only the first 2 kJ energy is plotted to clearly show the pickets.

safe environment. In contrast, both the baseline pulse and the acceleration-only pulse lack the plasma corona formation procedure.

Figure 7(b) confirms the necessity of a 'high foot' in the adiabat profile. For the two-picket pulse, the first picket produces an unsupported decaying shock[17] with minimal fuel heating. The second picket creates a slightly higher foot of $\alpha \sim 5$ to mitigate instability, and then the adiabat decreases to $\alpha \sim 2.5$, comparable to an isentropic drive. For the acceleration-only pulse, the already heavy imprint forces it to adopt a stronger shock, creating an $\alpha \sim 12$ 'ultra-high foot' that preserves the integrity of the shell

https://doi.org/10.1017/hpl.2023.35 Published online by Cambridge University Press

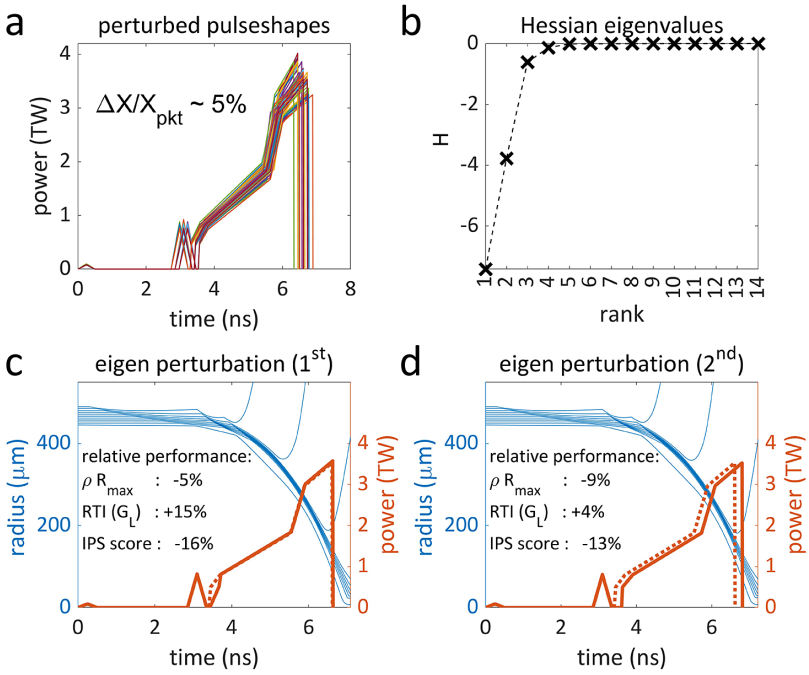

Figure 8. (a) Pulse shapes when 5% perturbation is added to the optimal two-picket pulse. (b) Eigenvalues of the IPS Hessian matrix. (c), (d) Pulse shapes and implosion streamlines after perturbation along the first and second eigenvectors. The dashed lines are the reference unperturbed pulse shapes.

through excessive amounts of thermal smoothing, but at the cost of areal density loss.

The improvement can be summarized as follows. The optimized pulse demonstrates a 16% increase in areal density (from 0.95 to 1.1 g/cm^2), a four-fold increase in the unmixed-fuel thickness (from 5 to 20 μm) and a superior adiabat shaping strategy relative to the baseline.

6.2. *Robustness of the optimization against shaping errors*

Real-world lasers inevitably contain shaping errors, and the effect of these errors on the optimization results can be assessed using Hessian matrix analysis. The Hessian is the Jacobian of the gradient of a scalar function $H = J(\nabla \mathrm{IPS})$. In our case, H describes the curvature of the IPS in pulse space, and the eigenvalues and eigenvectors of H reveal the sensitivity and robustness of the IPS to perturbations. Taking the two-picket pulse for example, Figure 8(b) shows that H is a negative-definite matrix, proving that the designer has indeed found the IPS local maximum.

The first two Hessian eigenvalues are significant. Their corresponding eigenvectors indicate two main descending directions of the IPS. Figures 8(c) and 8(d) show the perturbed pulses; the primary error is the rising slope at the acceleration, resulting in a 15% increase in the RTI. The secondary error is the time interval between the picket and the main pulse, resulting in a 9% decrease in the areal density. These results remind us to pay special attention to such shaping errors in real experiments.

6.3. *Optimization with and without seed correction*

Figure 9 shows a comparison of the pulse designs with and without seed correction. The uncorrected series tends to produce a more compact pulse sequence with a significantly shorter interval between the two pickets. However, the plasma scale length of the uncorrected series is too small and Figure 9(c) shows that the imprint suppression is insufficient. Figure 9(d) shows that the uncorrected pulse has a weaker stabilizing effect on the modes $L > 70$ and a higher risk of fuel mixing at the moment of extrusion.

In quantitative terms, inclusion of the seed correction reduces the perturbation intensity at short-to-medium wavelengths by 31% (averaged from $L = 100$ to $L = 500$) and the spectrum intensity of laser speckle by 40% (at the character mode $L = 150$).

The dominant instability mode of both series is $L \sim 45$. This is the combined result of the finite number of beams and the cone boundary. This long-wavelength perturbation is difficult to eliminate by pulse shaping alone. Our group is also working on high-Z-doping[35] and foam-coated targets[36] for DCI. It is hoped that this long-wavelength perturbation can be handled by joint optimization in the future.

7. Summary

We develop an automated pulse shape designer for improving the direct-drive implosion performance based on hydrodynamics simulations. This designer trains a machine-learning surrogate to predict the compression areal density

https://doi.org/10.1017/hpl.2023.35 Published online by Cambridge University Press

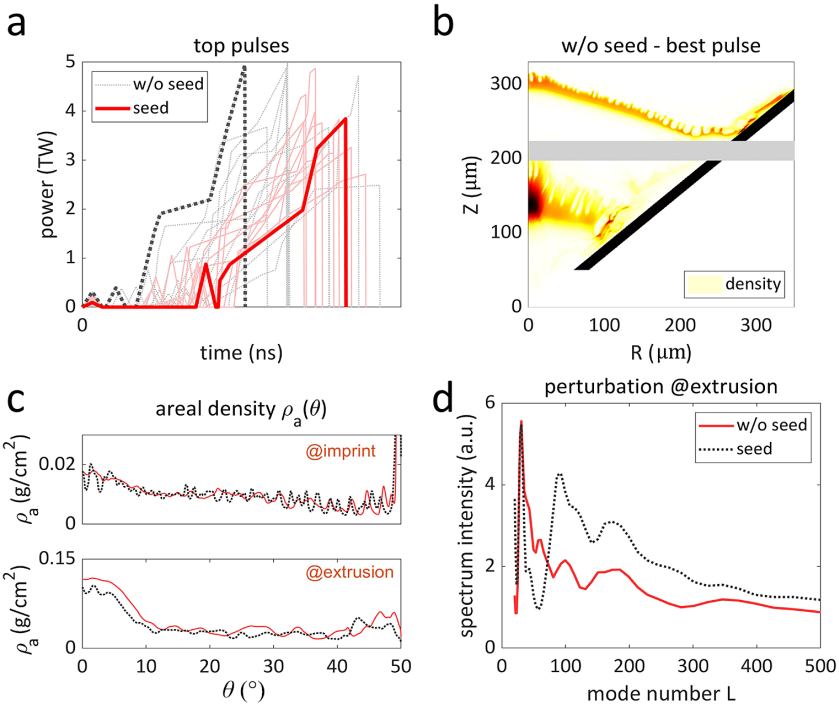

Figure 9. Optimized pulse series with and without imprint seed correction. (a) The best pulse in each series is shown with bold lines; the top 10 pulses in each series are shown with translucent lines. (b) Imploding shell density of the best pulse in the uncorrected series, taken at one-third and two-thirds of its initial radius. (c) Areal density perturbation of the two best pulses, where θ is the fuel polar angle. (d) Center-of-mass perturbation spectrum of the two best pulses.

and instability growth of a pulse shape, and operates the surrogate to optimize the pulse shape. The laser imprint and RTI linear growth are integrated into the optimization workflow through a prediction–correction alternation, enabling facility-specific engineering features such as laser speckles to be included in the instability estimation, making the pulse shaping more relevant and efficient. The designer is tested using the novel DCI direct-drive scheme. Simulations show that the optimized pulse increases the baseline areal density by 16% in one dimension, the clean-fuel thickness by a factor of four in two dimensions and the imprint resistance by over 30% in two dimensions. This pulse shape designer can be a useful tool for direct-drive ICF instability control.

Acknowledgement

This work is supported by the Strategic Priority Research Program of the Chinese Academy of Sciences (No. XDA25010200), the Fundamental Research Funds for the Central Universities (No. WK2140000014) and the DCI joint team.

References

1. J. Nuckolls, L. Wood, A. Thiessen, and G. Zimmerman, Nature **239**, 139 (1972).
2. R. Craxton, K. Anderson, T. Boehly, V. Goncharov, D. Harding, J. Knauer, R. McCrory, P. McKenty, D. Meyerhofer, J. Myatt, A. J. Schmitt, J. D. Sethian, R. W. Short, S. Skupsky, W. Theobald, W. L. Kruer, K. Tanaka, R. Betti, T. J. B. Collins, J. A. Delettrez, S. X. Hu, J. A. Marozas, A. V. Maximov, D. T. Michel, P. B. Radha, S. P. Regan, T. C. Sangster, W. Seka, A. A. Solodov, J. M. Soures, C. Stoeckl, and J. D. Zuegel, Phys. Plasmas **22**, 110501 (2015).
3. R. Betti and O. Hurricane, Nat. Phys. **12**, 435 (2016).
4. L. Rayleigh, Proc. London Math. Soc. **14**, 170 (1882).
5. G. I. Taylor, Proc. R. Soc. London Ser. A **201**, 192 (1950).
6. I. Igumenshchev, V. Goncharov, F. Marshall, J. Knauer, E. Campbell, C. Forrest, D. Froula, V. Y. Glebov, R. McCrory, S. Regan, T. C. Sangster, S. Skupsky, and C. Stoeckl, Phys. Plasmas **23**, 052702 (2016).
7. T. Ma, P. Patel, N. Izumi, P. Springer, M. Key, L. Atherton, M. Barrios, L. Benedetti, R. Bionta, E. Bond, D. K. Bradley, J. Caggiano, D. A. Callahan, D. T. Casey, P. M. Celliers, C. J. Cerjan, J. A. Church, D. S. Clark, E. L. Dewald, T. R. Dittrich, S. N. Dixit, T. Döppner, R. Dylla-Spears, D. H. Edgell, R. Epstein, J. Field, D. N. Fittinghoff, J. A. Frenje, M. Gatu Johnson, S. Glenn, S. H. Glenzer, G. Grim, N. Guler, S. W. Haan, B. A. Hammel, R. Hatarik, H. W. Herrmann, D. Hicks, D. E. Hinkel, L. F. Berzak Hopkins, W. W. Hsing, O. A. Hurricane, O. S. Jones, R. Kauffman, S. F. Khan, J. D. Kilkenny, J. L. Kline, B. Kozioziemski, A. Kritcher, G. A. Kyrala, O. L. Landen, J. D. Lindl, S. Le Pape, B. J. MacGowan, A. J. Mackinnon, A. G. MacPhee, N. B. Meezan, F. E. Merrill, J. D. Moody, E. I. Moses, S. R. Nagel, A. Nikroo, A. Pak, T. Parham, H.-S. Park, J. E. Ralph, S. P. Regan, B. A. Remington, H. F. Robey, M. D. Rosen, J. R. Rygg, J. S. Ross, J. D. Salmonson, J. Sater, D. Sayre, M. B. Schneider, D. Shaughnessy, H. Sio, B. K. Spears, V. Smalyuk, L. J. Suter, R. Tommasini, R. P. J. Town, P. L. Volegov, A. Wan, S. V. Weber, K. Widmann, C. H. Wilde, C. Yeamans, and M. J. Edwards, Phys. Plasmas **24**, 056311 (2017).

https://doi.org/10.1017/hpl.2023.35 Published online by Cambridge University Press

8. A. J. Schmitt, A. Velikovich, J. Gardner, C. Pawley, S. Obenschain, Y. Aglitskiy, and Y. Chan, Phys. Plasmas **8**, 2287 (2001).
9. D.-M. Ho, S. Haan, J. Salmonson, D. Clark, J. Lindl, J. Milovich, C. Thomas, L. B. Hopkins, and N. Meezan, J. Phys. Conf. Ser. **717**, 012023 (2016).
10. S. Skupsky and K. Lee, J. Appl. Phys. **54**, 3662 (1983).
11. J. Marozas, F. Marshall, R. Craxton, I. Igumenshchev, S. Skupsky, M. Bonino, T. Collins, R. Epstein, V. Y. Glebov, D. Jacobs-Perkins, J. P. Knauer, R. L. McCrory, P. W. McKenty, D. D. Meyerhofer, S. G. Noyes, P. B. Radha, T. C. Sangster, W. Seka, and V. A. Smalyuk, Phys. Plasmas **13**, 056311 (2006).
12. J. E. Rothenberg, J. Opt. Soc. Am. B **14**, 1664 (1997).
13. V. Goncharov, J. Knauer, P. McKenty, P. Radha, T. Sangster, S. Skupsky, R. Betti, R. McCrory, and D. Meyerhofer, Phys. Plasmas **10**, 1906 (2003).
14. T. Dittrich, O. Hurricane, D. Callahan, E. Dewald, T. Döppner, D. Hinkel, L. B. Hopkins, S. Le Pape, T. Ma, J. Milovich, J. C. Moreno, P. K. Patel, H.-S. Park, B. A. Remington, J. D. Salmonson, and J. L. Kline, Phys. Rev. Lett. **112**, 055002 (2014).
15. R. Kidder, Nucl. Fusion **16**, 3 (1976).
16. J. H. Gardner, S. E. Bodner, and J. P. Dahlburg, Phys. Fluids B **3**, 1070 (1991).
17. I. Igumenshchev, A. Velikovich, V. Goncharov, R. Betti, E. Campbell, J. Knauer, S. Regan, A. Schmitt, R. Shah, and A. Shvydky, Phys. Rev. Lett. **123**, 065001 (2019).
18. D. S. Clark, S. W. Haan, and J. D. Salmonson, Phys. Plasmas **15**, 056305 (2008).
19. S. Haan, J. Lindl, D. Callahan, D. Clark, J. Salmonson, B. Hammel, L. Atherton, R. Cook, M. Edwards, S. Glenzer, A. V. Hamza, S. P. Hatchett, M. C. Herrmann, D. E. Hinkel, D. D. Ho, H. Huang, O. S. Jones, J. Kline, G. Kyrala, O. L. Landen, B. J. MacGowan, M. M. Marinak, D. D. Meyerhofer, J. L. Milovich, K. A. Moreno, E. I. Moses, D. H. Munro, A. Nikroo, R. E. Olson, K. Peterson, S. M. Pollaine, J. E. Ralph, H. F. Robey, B. K. Spears, P. T. Springer, L. J. Suter, C. A. Thomas, R. P. Town, R. Vesey, S. V. Weber, H. L. Wilkens, and D. C Wilson, Phys. Plasmas **18**, 051001 (2011).
20. P. W. Hatfield, J. A. Gaffney, G. J. Anderson, S. Ali, L. Antonelli, S. B. du Pree, J. Citrin, M. Fajardo, P. Knapp, B. Kettle, B. Kustowski, M. J. MacDonald, D. Mariscal, M. E. Martin, T. Nagayama, C. A. J. Palmer, J. L. Peterson, S. Rose, J. J. Ruby, C. Shneider, M. J. V. Streeter, W. Trickey, and B. Williams, Nature **593**, 351 (2021).
21. P. Hatfield, S. Rose, and R. Scott, Phys. Plasmas **26**, 062706 (2019).
22. F. Wu, X. Yang, Y. Ma, Q. Zhang, Z. Zhang, X. Yuan, H. Liu, Z. Liu, J. Zhong, J. Zheng, and J. Zhang, High Power Laser Sci. Eng. **10**, e12 (2022).
23. S. Rose, P. Hatfield, and R. Scott, Philos. Trans. R. Soc. A **378**, 20200014 (2020).
24. J. L. Peterson, K. Humbird, J. E. Field, S. T. Brandon, S. H. Langer, R. C. Nora, B. K. Spears, and P. Springer, Phys. Plasmas **24**, 032702 (2017).
25. M. Martin, R. London, S. Goluoglu, and H. Whitley, High Energy Density Phys. **26**, 26 (2018).
26. V. Gopalaswamy, R. Betti, J. Knauer, N. Luciani, D. Patel, K. Woo, A. Bose, I. Igumenshchev, E. Campbell, K. Anderson, K. A. Bauer, M. J. Bonino, D. Cao, A. R. Christopherson, G. W. Collins, T. J. B. Collins, J. R. Davies, J. A. Delettrez, D. H. Edgell, R. Epstein, C. J. Forrest, D. H. Froula, V. Y. Glebov, V. N. Goncharov, D. R. Harding, S. X. Hu, D. W. Jacobs-Perkins, R. T. Janezic, J. H. Kelly, O. M. Mannion, A. Maximov, F. J. Marshall, D. T. Michel, S. Miller, S. F. B. Morse, J. Palastro, J. Peebles, P. B. Radha, S. P. Regan, S. Sampat, T. C. Sangster, A. B. Sefkow, W. Seka, R. C. Shah, W. T. Shmyada, A. Shvydky, C. Stoeckl, A. A. Solodov, W. Theobald, J. D. Zuegel, M. Gatu Johnson, R. D. Petrasso, C. K. Li, and J. A. Frenje, Nature **565**, 581 (2019).
27. K. D. Humbird, J. L. Peterson, B. Spears, and R. G. McClarren, IEEE Trans. Plasma Sci. **48**, 61 (2019).
28. B. Kustowski, J. A. Gaffney, B. K. Spears, G. J. Anderson, J. J. Thiagarajan, and R. Anirudh, IEEE Trans. Plasma Sci. **48**, 46 (2019).
29. J. Zhang, W. Wang, X. Yang, D. Wu, Y. Ma, J. Jiao, Z. Zhang, F. Wu, X. Yuan, Y. Li, and J. Q. Zhu, Philos. Trans. R. Soc. A **378**, 20200015 (2020).
30. R. Ramis, R. Schmalz, and J. Meyer-ter Vehn, Comput. Phys. Commun. **49**, 475 (1988).
31. B. Fryxell, K. Olson, P. Ricker, F. Timmes, M. Zingale, D. Lamb, P. MacNeice, R. Rosner, J. Truran, and H. Tufo, Astrophys. J. Suppl. Ser. **131**, 273 (2000).
32. R. Betti, V. Goncharov, R. McCrory, and C. Verdon, Phys. Plasmas **5**, 1446 (1998).
33. S. Suthaharan and S. Suthaharan, in *Machine Learning Models and Algorithms for Big Data Classification: Thinking with Examples for Effective Learning* (Springer, New York, 2016), p. 207.
34. A. Likas, N. Vlassis, and J. J. Verbeek, Pattern Recogn. **36**, 451 (2003).
35. G. Zheng, T. Tao, Q. Jia, R. Yan, and J. Zheng, Plasma Phys. Control. Fusion **64**, 105003 (2022).
36. D. Liu, T. Tao, J. Li, Q. Jia, and J. Zheng, Phys. Plasmas **29**, 072707 (2022).

https://doi.org/10.1017/hpl.2023.35 Published online by Cambridge University Press